nature structural & molecular biology

Structural basis of Nipah and Hendra virus attachment to their cell-surface receptor ephrin-B2

Thomas A Bowden, A Radu Aricescu, Robert J C Gilbert, Jonathan M Grimes, E Yvonne Jones & David I Stuart

Nipah and Hendra viruses are emergent paramyxoviruses, causing disease characterized by rapid onset and high mortality rates, resulting in their classification as Biosafety Level 4 pathogens. Their attachment glycoproteins are essential for the recognition of the cell-surface receptors ephrin-B2 (EFNB2) and ephrin-B3 (EFNB3). Here we report crystal structures of both Nipah and Hendra attachment glycoproteins in complex with human EFNB2. In contrast to previously solved paramyxovirus attachment complexes, which are mediated by sialic acid interactions, the Nipah and Hendra complexes are maintained by an extensive protein-protein interface, including a crucial phenylalanine side chain on EFNB2 that fits snugly into a hydrophobic pocket on the viral protein. By analogy with the development of antivirals against sialic acid binding viruses, these results provide a structural template to target antiviral inhibition of protein-protein interactions.

Nipah (NiV) and Hendra (HeV) viruses are recent additions[1] to a growing number of emergent disease agents that use bats as a natural host. Sole members of the genus Henipavirus, within the family *Paramyxoviridae*, HeV and NiV were discovered in 1994 and 1999, respectively, and are zoonotic and extremely pathogenic[2–4]. Outbreaks have been reported throughout Southeast Asia and Australia, characterized by a high level of respiratory distress and a patient fatality rate approaching 75%, with death occurring 7–10 d after infection[5]. These viruses are also threats to livestock; one Nipah outbreak in Malaysia resulted in the culling of more than 1 million pigs[6]. As a result of the persistent and harmful threat that these viruses pose, they are currently the target of major efforts to characterize and develop immunotherapeutics and antiviral drugs[7–9].

The recent discovery of EFNB2 and EFNB3 as the cellular receptors for these viruses' attachment glycoproteins is an important step toward combating these pathogens, as it explains the tropism of the viruses (correlating with their broad host range and respiratory and neurological pathology[10–12]) and identifies targets for antiviral drug design[10]. EFNs are attached to the cell membrane, consist of a single extracellular domain with a Greek key β-barrel fold and are involved in developmental and neurological processes such as boundary formation, cell migration and axonal guidance[13]. Recent crystal structures of EFNs in complex with their cognate EPH receptors have provided much information about the molecular details that govern their specificity and allowed the development of reagents that can modulate EFN–EPH receptor interactions[14–18].

The HeV and NiV attachment glycoproteins that bind to EFNB2 and EFNB3, HeV-G and NiV-G, are type II integral membrane proteins consisting of an N-terminal cytoplasmic tail, a single transmembrane helix, a stalk region and a C-terminal six-bladed β-propeller. HeV and NiV are similar to Measles virus, Canine distemper virus and Rinderpest virus in that they enter cells by binding glycoproteins in a sialic acid–independent manner using a mechanism to promote cell fusion by the F protein, whereas other members of the *Paramyxoviridae* family (for example, Parainfluenza and Newcastle disease viruses) attach via sialic acid[19–21]. Much research has focused on identifying the residues required for the EFN-virus interaction, resulting in a preliminary localization of the viral-EFN binding interface[22–24].

In this study, we sought to ascertain the mechanism by which NiV and HeV viruses attach to EFN ligands. Crystal structures of NiV-G and HeV-G glycoproteins in complex with human EFNB2 ligand allow us to identify unexpected aspects of the specificity of this interaction, which we confirm via biophysical studies, and this exposes targets for the development of antiviral antagonists. Additionally, analyses of these complexes reveal distinct structural changes that have allowed HeV and NiV to switch from host attachment via sialic acid (as used by the closely related parainfluenza viruses) to attachment via a protein-protein interaction. This structural adaptation provides a rationale for the emergence of these new and dangerous viruses.

RESULTS

Structure of NiV-G–EFNB2 and HeV-G–EFNB2 complexes

For structural analysis, the globular β-propeller ectodomain of NiV-G (residues 183–602) and the full-length ectodomain portion of HeV-G (residues 71–604), which also includes the N-terminal stalk domain, were coexpressed with EFNB2 in HEK293T cells[25] in the presence of kifunensine[26], and resultant oligomannose-type glycans were trimmed to single *N*-acetylglucosamine moieties using endoglycosidase F1

Division of Structural Biology, University of Oxford, Henry Wellcome Building of Genomic Medicine, Roosevelt Drive, Oxford OX3 7BN, UK. Correspondence should be addressed to D.I.S. (dave@strubi.ox.ac.uk).

Received 6 December 2007; accepted 28 April 2008; published online 18 May 2008; doi:10.1038/nsmb.1435

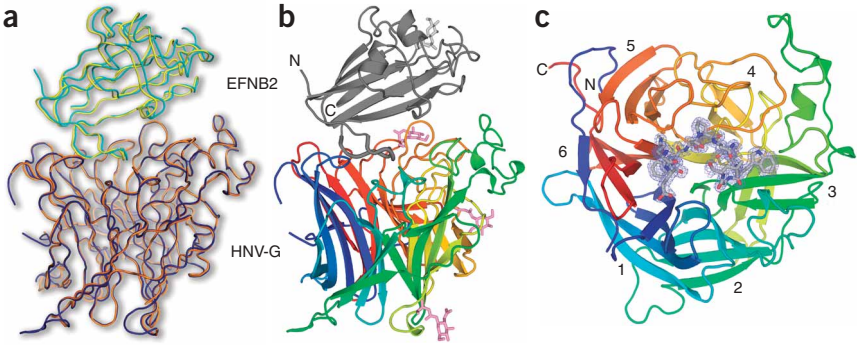

Figure 1 NiV-G–EFNB2 and HeV-G–EFNB2 complex structures. (**a**) Cα trace representations of NiV-G–EFNB2 (1.8-Å resolution; NiV-G is blue and EFNB2 is yellow) and HeV-G–EFNB2 (3.3-Å resolution; HeV-G is orange and EFNB2 is cyan) superimposed on the viral receptor component of the complexes. The structures of NiV-G and HeV-G in complex with EFNB2 are practically identical (0.5-Å r.m.s. deviation in equivalent Cα atoms over residues 189–601). As a result, subsequent figures show the higher-resolution NiV-G–EFNB2 structure, and it will be referred to generically as HNV-G. (**b**) Cartoon diagram of HNV-G–EFNB2 (colored as a rainbow with the N terminus in blue and the C terminus in red) in complex with EFNB2 ligand (gray). *N*-acetylglucosamine moieties observed as stubs at the N-linked glycosylation sites in the NiV-G–EFNB2 structure are shown as sticks (pink). (**c**) Looking down the six-fold β-propeller of HNV-G with $2F_o - F_c$ electron density (blue mesh, 1.0 σ) and EFNB2 residues 118–126 from the G-H binding loop shown.

(**Supplementary Fig. 1** online). Crystal structures of these complexes were determined at 1.8-Å and 3.3-Å resolution, respectively (**Methods**, **Fig. 1a**, **Supplementary Fig. 2** and **Supplementary Table 1** online).

NiV-G and HeV-G are extremely similar in structure (0.5-Å r.m.s. deviation in their Cα atoms over residues 189–601, only slightly higher than the 0.3-Å r.m.s. deviation between the EFN moieties bound to the different G proteins), as expected for proteins that share 81% sequence identity. We will therefore, as appropriate, refer to these generically as HNV-G. The six-bladed β-propeller domain of HNV-G forms a 1:1 complex with EFNB2. Although these domains are monomeric (**Supplementary Fig. 3a** online), we found that the full-length ectodomain portion of HNV-G, which includes the N-terminal stalk domain (**Supplementary Fig. 3b**), self-associates to form higher-order oligomers, as observed for Parainfluenza virus III (PIV-III)[19], Parainfluenza virus V (PIV-V)[21], Newcastle disease virus (NDV)[20] hemagglutinin-neuraminidases and Measles virus hemagglutinin (MV-H)[27,28]. Although crystallization experiments of HeV-G–EFNB2 included the full-length ectodomain (with stalk region), we did not see the stalk or molecular contacts consistent with oligomers in the HeV-G–EFNB2 crystal structure. Therefore, it is likely that the stalk domain was cleaved during crystallization.

The mode of engagement of the EFNB2 with both NiV-G and HeV-G is the same, with only a 3.5° change in the relative orientation of the EFN (**Fig. 1a**). The EFNB2 contribution to the complex occurs overwhelmingly via the residues in, and surrounding, the G-H loop (residues 107–125, **Supplementary Fig. 4** online), which inserts into a central depression in the upper surface of the viral G protein β-propeller (**Fig. 1b,c**). This corresponds to the face of the β-propeller, which harbors the sialic acid binding site in PIV and NDV hemagglutinin-neuraminidases[19–21]. The large interface is consistent with the high affinity (~1 nM) of HNV-G–EFNB2 interactions[11,12]; which are more than an order of magnitude tighter than other examples of paramyxovirus receptor interactions such as MV-H–SLAM and MV-H–CD46 (ref. 29). The HNV-G–EFNB2 interaction is entirely protein-protein; we observed electron density for *N*-acetylglucosamine at three out of five and one out of two predicted *N*-linked glycosylation sites on NiV-G and EFNB2, respectively, but none of these contributed to the HNV-G–EFNB2 interaction (**Fig. 1b**).

The β-propeller fold of HNV-G consists of four antiparallel β-strands per blade and is similar to those previously reported for PIV-III[19], PIV-V[21], NDV[20] and MV-H proteins[27,28]. Although the hydrophobic cores are similar, the wings and variable surface regions of HNV-G differ substantially in comparison with the other structures, the closest match being for PIV-III (2.5-Å r.m.s. deviation over 387 matching Cα atoms; **Supplementary Fig. 5a** online). The site of EFNB2 binding to HNV-G varies markedly in character from the previously identified sialic acid binding sites in the PIV-III, PIV-V and

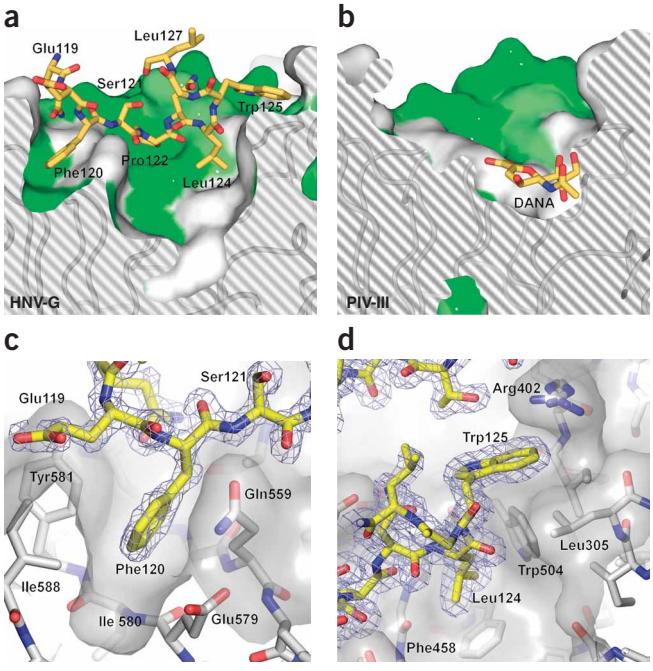

Figure 2 Comparison of protein-protein and protein-sugar interactions required for paramyxovirus attachment and fusion. (**a**) Slab through the van der Waals surface of NiV-G interfaced with the EFNB2 binding loop residues Glu119–Trp125. The green surface corresponds to amino acids conserved in sequence between PIV-III and HNV-G, whereas white areas are not conserved. (**b**) Slab through the van der Waals surface of PIV-III with bound sialic acid analog (DANA, PDB 1V3D; surfaces colored as in **a**). (**c**) Phe120 of EFNB2 is essential for binding, is buried deeply into a pocket and interacts with Tyr581, Ile588, Gln559 and Glu579 on HNV-G (gray van der Waals surface). (**d**) Trp125 and Leu124 of EFNB2 are necessary for HNV-G binding[11] and are bound to a highly hydrophobic surface of HNV-G that includes Trp504, Phe458 and Leu305 (gray van der Waals surface).

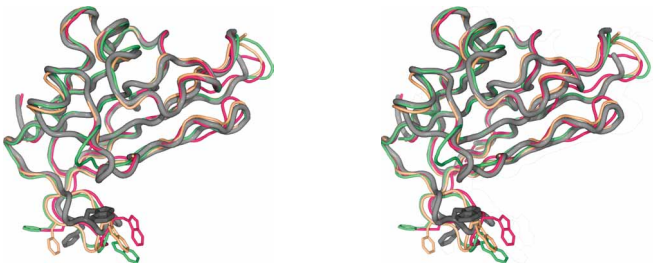

Figure 3 Conformational changes that occur to the EFNB2 G-H loop upon receptor binding. EFNB2 bound to HNV-G is shown as a gray cartoon in stereo. EFNB2 in its apo form (PDB 1IKO; 1.9-Å r.m.s. deviation over 138 equivalent Cα atoms) is red, EFNB2 bound to EPHB2 (PDB 1NUK; 2.0-Å r.m.s. deviation over 136 equivalent Cα atoms) is green, and EFNB2 when bound to EPHB4 (PDB 2HLE, 2.0-Å r.m.s. deviation over 136 equivalent Cα atoms) is orange. Trp125^{EFNB2} and Phe120^{EFNB2} are shown as sticks to illustrate positional differences of EFNB2 in apo, EPHB4-, EPHB2- and HNV-G–bound forms.

NDV hemagglutinin-neuraminidases (**Fig. 2**). In HNV-G the EFNB2 binding interface is relatively flat (**Fig. 2a**), whereas in PIV and NDV (**Fig. 2b**) sialic acid binds much more deeply into the center of the β-propeller; however, HNV-G does retain a marked 'cleft' homologous to the sialic acid binding pocket. Thus, although there is currently no evidence that HNV-G binds sialic acid, a secondary binding activity cannot be discounted, and low-affinity interactions with a high-abundance receptor such as sialic acid could help to localize viruses to the cell surface and facilitate interactions with the high-affinity, but less abundant, EFNB2 receptor. It is intriguing that the structures closest to HNV-G are sialic acid binding parainfluenza virus attachment proteins (**Supplementary Fig. 5a**), rather than the other protein binder, MV-H (**Supplementary Fig. 5b**, 3.3-Å r.m.s. deviation over 323 matching Cα atoms)[27,28]. A structure-based phylogeny of these proteins (**Supplementary Fig. 5c**) suggests that the switch to protein-protein attachment has occurred more than once during the evolution of the parainfluenza viruses.

The overall structure of EFNB2 bound to HNV-G remains similar to the apo structure[30] (1.9-Å r.m.s. deviation over 138 equivalent Cα atoms), and the EPH receptor B2 (EPHB2)-bound[14] (2.0-Å r.m.s. deviation over 136 equivalent Cα atoms) and EPHB4-bound[17] (1.7-Å r.m.s. deviation over 132 equivalent Cα atoms) forms[31]. However, there are clear changes in the conformation of the G-H loop, which is central to both the EPH–EFN and HNV-G–EFN interactions (**Fig. 3**). Trp125^{EFNB2}, for example, which is present on this loop and key to both EPH and HNV-G interactions, varies in position by a distance of less than 3.8 Å in the apo, EPHB2- and EPHB4-bound forms, whereas it is rearranged substantially when bound to HNV-G (average distance >8 Å from other EFNB2 structures). This change in loop conformation shows the plasticity of EFN ligands and demonstrates how the flexibility of a particular binding loop can provide specificity for dissimilar binding sites.

The HNV-G–EFNB2 interface

The surface area buried in the HNV-G–EFNB2 complexes is more extensive than that of EFNB2 bound to its cognate human cell-surface receptor (EPH), with buried surface areas of 2,800 Å^2 (surface complementarity[32], sc = 0.78) and 2,700 Å^2 (sc = 0.69) for NiV-G and HeV-G, respectively, compared to the average buried surface area of 2,250 Å^2 (average sc = 0.66) for published EPH–EFNB2 structures[14,17] (**Fig. 4a**). The high degree of sequence and structural conservation of the EFNB2 binding site on HNV-G structures (**Fig. 4b** and **Supplementary Fig. 6** online) reflects a functional constraint and also the close evolutionary link between the two viruses. The only sequence difference between NiV-G and HeV-G in a residue directly involved in the EFNB2 binding interface is a valine to threonine change at residue 507. This residue makes van der Waals interactions with Pro122, which is conserved in EFNB3. This is in-line with the observed loss of binding affinity for a Ser507 variant[24]; however, the structural data cannot explain the reported difference in specificity for the two EFNs conferred by the valine to threonine change in the viral proteins[24]. Similarly, the residues responsible for the interaction with the viral protein are conserved between EFNB2 and EFNB3 in humans and across species (**Supplementary Fig. 6a**), consistent with the recently reported ability of HeV and NiV to infect cells expressing EFNB2 and EFNB3 from a broad range of species[33].

The NiV-G–EFNB2 interface is largely conserved in the HeV-G–EFNB2 complex and helps rationalize many of the previously reported functional data[22–24]. In particular, there is excellent agreement with the results of Guillaume *et al.*[23] and Negrete *et al.*[24]; however the residues identified by Bishop *et al.*[22] are away from the EFN binding site and are likely to simply stabilize the β-propeller fold (**Supplementary Fig. 7** online). The interface comprises 24 hydrogen bonds (involving 17 residues on NiV-G and 14 residues on EFNB2), 4 salt bridges (two residues on NiV-G and three residues on EFNB2) and several key hydrophobic interactions. As predicted by previously reported mutagenesis studies, Leu124^{EFNB2} and Trp125^{EFNB2} have an important role[11] in forming van der Waals interactions with Phe458

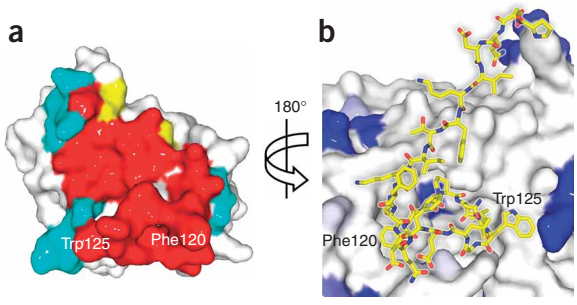

	EFNB2-wt	F120Y^{EFNB2}
k_a (Ms^{-1})	3.4×10^5	3.4×10^5
k_d (s^{-1})	1.1×10^{-2}	7.0×10^{-2}
K_d (nM)	35	86
χ^2	3.5	2.0

Figure 4 Points of molecular specificity in the HNV-G–EFNB2 interaction. (**a**) Comparison between buried surface of EFNB2 in the EPHB4–EFNB2[17] and HNV-G–EFNB2 complexes. Surfaces for EFNB2 residues buried in both complexes are red, residues buried only in HNV-G are cyan and residues buried only in EPHB4 are yellow. Surfaces for noninteracting residues are white. (**b**) EFNB2 residues 107–127 (sticks colored as in **Figure 2**) in complex with NiV-G (van der Waals surface colored according to residue conservation with HeV-G: white, conserved; light blue, similar; blue, no sequence conservation). (**c**) K_d determination for binding between NiV-G and wild-type EFNB2 (EFNB2-wt) or F120Y^{EFNB2} using surface plasmon resonance. Responses were recorded for EFNB2-wt and F120Y^{EFNB2} injected over immobilized, monomeric NiV-G during association and dissociation phases with analyte concentrations ranging from 5–100 nM. F120A^{EFNB2} and F120E^{EFNB2} mutations were also tested but showed no detectable binding to NiV-G. k_a, k_d, K_d and χ^2 values were averaged over six separate kinetic experiments for the interaction of wild-type NiV-G with EFNB2 and two experiments for NiV-G with F120Y^{EFNB2}.

Table 1 Data collection and refinement statistics

	NiV-G–EFNB2	HeV-G–EFNB2
Data collection		
Space group	$P2_12_12_1$	$P2_12_12_1$
Cell dimensions		
a, *b*, *c* (Å)	63.2, 95.8, 97.9	56.3, 106.2, 196.2
Resolution (Å)	30 (1.8)[a]	30 (3.3)
R_{merge}	8.6 (52.5)	20.1 (35.6)
$I / \sigma I$	15.0 (2.3)	6.1 (2.9)
Completeness (%)	98.9 (90.4)	93.3 (87.3)
Redundancy	6.9 (5.5)	7.6 (5.5)
Refinement		
Resolution (Å)	30–1.8	20.0–3.3
No. reflections	55,100	17,117
R_{work} / R_{free}	15.2/19.8	30.0/35.0
No. atoms		
Protein	4,507	8,443
Ligand/ion	60	0
Water	705	0
B-factors		
Protein	14.6	34.3
Ligand/ion	27.4	N/A
Water	27.0	N/A
R.m.s. deviations		
Bond lengths (Å)	0.013	0.017
Bond angles (°)	1.5	2.5

[a]Values in parentheses are for highest-resolution shell.

and Trp504, respectively (**Fig. 2d**). In addition, Phe120^{EFNB2} is completely buried in a conserved hydrophobic pocket on NiV-G and HeV-G (**Fig. 2c**). This is noteworthy, as Phe120^{EFNB2} shows only a limited role in EPH–EFN interfaces and thus represents an attractive potential drug target. To assess whether Phe120^{EFNB2} is essential and provides specificity for the interaction, we prepared site-directed EFNB2 mutants: F120Y^{EFNB2}, F120A^{EFNB2} and F120E^{EFNB2}. Kinetic measurements of wild-type EFNB2 binding to NiV-G (calculated using a 1:1 Langmuir model) gave a K_d of 35 nM (**Fig. 4** and **Supplementary Fig. 8a** online), slightly stronger than that for the F120Y^{EFNB2} mutant (86 nM; **Fig. 4** and **Supplementary Fig. 8b**), consistent with the presence of a tyrosine at this position in EFNB3. These binding constants are weaker than previously published results, a discrepancy that may be due to the present measurements being done with monomeric proteins[10,11,34]. In contrast, F120A^{EFNB2} and F120E^{EFNB2} showed no binding to NiV-G. These results suggest that this pocket might be a viable target for structure-based drug design.

DISCUSSION

It is now clear that the paramyxoviruses share glycoproteins of common architecture, a six-bladed β-propeller, no matter whether they attach through sialic acid–dependent or –independent mechanisms. In evolutionary terms, the ancestral viruses presumably used this protein as a neuraminidase and may well have had a separate attachment protein. The acquisition of novel protein binding sites (that do not use the deep sialic acid binding pockets), would provide a natural route for the emergence of new viruses, and potentially serious diseases. The use of high-affinity interactions with relatively low-abundance cell-surface glycoproteins as receptors removes the need for a receptor-releasing enzyme to facilitate effective virus spread from cell to cell. Although such emergent, highly pathogenic viruses are cause for serious concern, the protein-protein interactions they rely on for cell entry may be targeted by antiviral compounds, designed in a fashion analogous to that exploited successfully for the blockade of sialic acid binding sites by antiviral therapeutics[35].

METHODS

Protein expression and purification. HeV-G (residues 71–604, GenBank NC_001906, synthesized by GeneArt, LTD), NiV-G (residues 183–602, GenBank NC_002728, GeneArt, LTD) and EFNB2 (residues 25–168, GenBank NM_004093, obtained by RT-PCR from a human brain mRNA sample, Clonetech) were cloned into the pHLsec vector[25] and transiently coexpressed in HEK293T cells in the presence of the class I α-mannosidase inhibitor, kifunensine[26], with 2 mg DNA per liter of cell culture in a 3:1 ratio of HeV-G and NiV-G to EFNB2 ligand. Both complexes were purified by immobilized metal-affinity chromatography (IMAC) and then treated with endoglycosidase F1 (75 μg mg^{-1} protein, 12 h, 21 °C) to cleave glycosidic bonds of *N*-linked sugars within the di-*N*-acetylchitebiose core. Following deglycosylation, protein complexes were purified by size-exclusion chromatography using a Superdex 200 10/30 column (Amersham), in 150 mM NaCl, 10 mM Tris, pH 8.0, buffer. Protein yields were typically 2 mg deglycosylated HNV-G–EFNB2 complex per liter of cell culture.

Analytical ultracentrifugation. Sedimentation equilibrium measurements were performed using a Beckman Optima XL-I analytical ultracentrifuge (AUC) using absorbance optics with baseline absorbance determined at 1.290×10^4 *g*. Before AUC, proteins were purified by IMAC and further by size-exclusion chromatography. AUC runs of fully glycosylated proteins were run in size-exclusion buffer (above). For the NiV-G construct containing only the β-propeller domain, we used rates of 8.1×10^3 *g*, 1.5×10^4 *g* and 2.5×10^4 *g*, and for full-length NiV–G complexed with EFNB2 we used rates of 5.1×10^3 *g*, 8.9×10^3 *g* and 1.6×10^4 *g*. For the NiV-G–EFNB2 complex, two peaks eluted from gel filtration were run individually. Data were analyzed using UltraSpin[36] with a single-species model calculating whole-cell weight-average molecular weights, which then indicate self-association or nonideality in their systematic variation over concentration and speed ranges.

Site-directed mutagenesis. Mutations designed to test for specificity of Phe120^{EFNB2} (F120Y^{EFNB2}, F120A^{EFNB2} and F120E^{EFNB2}) were generated using a two-step overlapping PCR experiment (Pyrobest Polymerase, Takara). PCR product was cloned into the pHLsec mammalian expression vector. All constructs (wild type and mutants) were verified by DNA sequencing.

Crystallization and structure determination. Crystals were grown by sitting drop vapor diffusion using 100 nL protein plus 100 nL precipitant as described previously[37]. NiV-G–EFNB2 complex crystals grew at 4 °C (8 mg ml^{-1}) in 18% (v/v) isopropanol, 18% (w/v) PEG 3350 and 0.1 M tricitrate buffer, pH 5.6, after 3 d. HeV-G–EFNB2 complex crystals grew at room temperature (10 mg ml^{-1}) after 21 d in 25% (w/v) PEG 3350 and 0.1 M bis-Tris, pH 5.5. Crystals were flash frozen by immersion of the crystal into a cryoprotectant containing 20% (v/v) glycerol (HeV-G–EFNB2) or perfluoropolyether oil PFO-X125/03 (Lancaster Synthesis) (NiV-G–EFNB2) followed by rapid transfer to a gaseous nitrogen stream. Data were collected at beamlines ID14-EH2 (NiV-G–EFNB2) and ID23.1 (HeV-G–EFNB2) at the European Synchrotron Radiation Facility (ESRF), France. Images were integrated and scaled using the programs DENZO and SCALEPACK[38] (for NiV-G–EFNB2) and XDS (for HeV-G–EFNB2)[39]. Details of crystallographic statistics and crystallization are presented in **Table 1** and **Supplementary Table 1**, respectively.

The structure of NiV-G–EFNB2 was solved by molecular replacement using the program Phaser[40] with EFNB2 (PDB 1NUK[14]) and PIV-III–HN (PDB 1V3E[19]) as the search models. The refined NiV-G–EFNB2 structure was used to solve (Phaser) the lower-resolution HeV-G–EFNB2 structure. For all structures, 5% of reflections were randomly set aside to calculate the R_{free}. Initial automatic model building for the high-resolution NiV-G–EFNB2 structure was performed with the program ARP-wARP[41]. Generally, structure refinement included iterative restrained refinement with TLS using REFMAC 5

and PHENIX[42–45]. The molecular graphics program COOT was used for all manual rebuilding[46]. The programs PROCHECK and WhatCheck were used to validate all models[47,48]. Ramachandran analysis of the NiV-G–EFNB2 structure showed that 86.3% of residues were in the most favored region, 12.8% of residues were in additionally allowed regions and 0.8% in the generously allowed region. Ramachandran analysis of the HeV-G–EFNB2 structure gave 75.7% of residues in the most favored region, 23.6% in additionally allowed regions and 1.1% in the generously allowed regions.

Binding studies. Target constructs were subcloned from the pHLsec vector into the pHLsec–avitag-3 vector[25]; a vector that expresses a 15-amino-acid peptide at the C-terminus of the protein recognized by biotin ligase (BirA). Proteins immobilized on chelating Sepharose Fast Flow Ni^{2+}-agarose beads (GE Healthcare) were biotinylated as described previously[49].

All proteins used during these binding studies had wild-type glycosylation. Surface plasmon resonance runs were performed using a BIAcore T100 (Biacore). Purified, biotinylated proteins were immobilized on a CM5 BIAcore sensor chip (Biacore) coated with streptavidin (Sigma). A surface with only streptavidin present on the chip was reserved to subtract background responses due to differences in refractive indices of running and sample buffers. For kinetic measurements of analyte binding to immobilized protein, samples were injected at 50 µl min^{-1} (25 °C) in HBS-EP buffer (10 mM HEPES, pH 7.4, 150 mM NaCl, 0.005% (v/v) surfactant P20 and 3 mM EDTA). To calculate the binding affinity of NiV-G to EFNB2, several cycles of association, dissociation and regeneration with 3 M $MgCl_2$ at different concentrations of analyte were required. Analyte concentrations ranged from 5–100 nM and K_{on}, K_{off} and K_d values were calculated using Biacore Evaluation Software Version 1.1.1 using a 1:1 Langmuir model.

Superimpositions. All molecular superimpositions were calculated using SHP[31].

Illustrations. All molecular representations were produced with PyMOL (http://pymol.sourceforge.net), and **Supplementary Figure 3** was produced with LIGPLOT[50]. Sequence alignments were performed with Multalign[51] and formatted with Espript[52]. Figures were prepared using Adobe Illustrator, Adobe Photoshop and Microsoft Publisher.

Accession codes. Protein Data Bank: Coordinates and structure factors of NiV-G–EFNB2 and HeV-G–EFNB2 have been deposited with accession codes 2VSM and 2VSK, respectively.

Note: Supplementary information is available on the Nature Structural & Molecular Biology website.

ACKNOWLEDGMENTS

We are grateful for the help of W. Lu in tissue culture, K. Harlos for data collection, C. O'Callaghan for discussions and the staff of beamlines ID14.2 and ID23.1 at the European Synchotron Radiation Facility for assistance. This work was funded by the Wellcome Trust, Medical Research Council, Royal Society, Cancer Research UK and Spine2 Complexes (FP6-RTD-031220).

AUTHOR CONTRIBUTIONS

T.A.B., A.R.A., J.M.G., E.Y.J. and D.I.S. contributed to the design of the project and preparation of the manuscript; T.A.B. was responsible for K_d determination. T.A.B. and A.R.A. were responsible for cloning and construct design; T.A.B. expressed, purified and crystallized the HNV-G complexes; T.A.B., J.M.G. and D.I.S. contributed to X-ray data collection and solving the structure of NiV-G–EFNB2 and HeV-G–EFNB2; T.A.B. and R.J.C.G. performed AUC analysis of NiV-G.

Published online at http://www.nature.com/nsmb/
Reprints and permissions information is available online at http://npg.nature.com/reprintsandpermissions/

1. Eaton, B.T., Broder, C.C., Middleton, D. & Wang, L.F. Hendra and Nipah viruses: different and dangerous. *Nat. Rev. Microbiol.* **4**, 23–35 (2006).
2. Parashar, U.D. *et al.* Case-control study of risk factors for human infection with a new zoonotic paramyxovirus, Nipah virus, during a 1998–1999 outbreak of severe encephalitis in Malaysia. *J. Infect. Dis.* **181**, 1755–1759 (2000).
3. Selvey, L.A. *et al.* Infection of humans and horses by a newly described morbillivirus. *Med. J. Aust.* **162**, 642–645 (1995).
4. Murray, K. *et al.* A morbillivirus that caused fatal disease in horses and humans. *Science* **268**, 94–97 (1995).
5. Hsu, V.P. *et al.* Nipah virus encephalitis reemergence, Bangladesh. *Emerg. Infect. Dis.* **10**, 2082–2087 (2004).
6. Mohd Nor, M.N., Gan, C.H. & Ong, B.L. Nipah virus infection of pigs in peninsular Malaysia. *Rev. Sci. Tech.* **19**, 160–165 (2000).
7. Guillaume, V. *et al.* Nipah virus: vaccination and passive protection studies in a hamster model. *J. Virol.* **78**, 834–840 (2004).
8. Guillaume, V. *et al.* Antibody prophylaxis and therapy against Nipah virus infection in hamsters. *J. Virol.* **80**, 1972–1978 (2006).
9. Bossart, K.N. & Broder, C.C. Developments towards effective treatments for Nipah and Hendra virus infection. *Expert Rev. Anti Infect. Ther.* **4**, 43–55 (2006).
10. Negrete, O.A. *et al.* EphrinB2 is the entry receptor for Nipah virus, an emergent deadly paramyxovirus. *Nature* **436**, 401–405 (2005).
11. Negrete, O.A. *et al.* Two key residues in ephrinB3 are critical for its use as an alternative receptor for Nipah virus. *PLoS Pathog.* **2**, e7 (2006).
12. Bonaparte, M.I. *et al.* Ephrin-B2 ligand is a functional receptor for Hendra virus and Nipah virus. *Proc. Natl. Acad. Sci. USA* **102**, 10652–10657 (2005).
13. Wilkinson, D.G. Multiple roles of EPH receptors and ephrins in neural development. *Nat. Rev. Neurosci.* **2**, 155–164 (2001).
14. Himanen, J.P. *et al.* Crystal structure of an Eph receptor-ephrin complex. *Nature* **414**, 933–938 (2001).
15. Himanen, J.P. *et al.* Repelling class discrimination: ephrin-A5 binds to and activates EphB2 receptor signaling. *Nat. Neurosci.* **7**, 501–509 (2004).
16. Chrencik, J.E. *et al.* Structure and thermodynamic characterization of the EphB4/Ephrin-B2 antagonist peptide complex reveals the determinants for receptor specificity. *Structure* **14**, 321–330 (2006).
17. Chrencik, J.E. *et al.* Structural and biophysical characterization of the EphB4-ephrinB2 protein-protein interaction and receptor specificity. *J. Biol. Chem.* **281**, 28185–28192 (2006).
18. Chrencik, J.E. *et al.* Three dimensional structure of the EPHB2 receptor in complex with an antagonistic peptide reveals a novel mode of inhibition. *J. Biol. Chem.* **282**, 36505–36513 (2007).
19. Lawrence, M.C. *et al.* Structure of the haemagglutinin-neuraminidase from human parainfluenza virus type III. *J. Mol. Biol.* **335**, 1343–1357 (2004).
20. Crennell, S., Takimoto, T., Portner, A. & Taylor, G. Crystal structure of the multi-functional paramyxovirus hemagglutinin-neuraminidase. *Nat. Struct. Biol.* **7**, 1068–1074 (2000).
21. Yuan, P. *et al.* Structural studies of the parainfluenza virus 5 hemagglutinin-neuraminidase tetramer in complex with its receptor, sialyllactose. *Structure* **13**, 803–815 (2005).
22. Bishop, K.A. *et al.* Identification of Hendra virus g glycoprotein residues that are critical for receptor binding. *J. Virol.* **81**, 5893–5901 (2007).
23. Guillaume, V. *et al.* Evidence of a potential receptor-binding site on the Nipah virus G protein (NiV-G): identification of globular head residues with a role in fusion promotion and their localization on an NiV-G structural model. *J. Virol.* **80**, 7546–7554 (2006).
24. Negrete, O.A., Chu, D., Aguilar, H.C. & Lee, B. Single amino acid changes in the Nipah and Hendra virus attachment glycoprotein distinguishes ephrinB2 from ephrinB3 usage. *J. Virol.* **81**, 10804–10814 (2007).
25. Aricescu, A.R., Lu, W. & Jones, E.Y. A time- and cost-efficient system for high-level protein production in mammalian cells. *Acta Crystallogr. D Biol. Crystallogr.* **62**, 1243–1250 (2006).
26. Chang, V.T. *et al.* Glycoprotein structural genomics: solving the glycosylation problem. *Structure* **15**, 267–273 (2007).
27. Hashiguchi, T. *et al.* Crystal structure of measles virus hemagglutinin provides insight into effective vaccines. *Proc. Natl. Acad. Sci. USA* **104**, 19535–19540 (2007).
28. Colf, L.A., Juo, Z.S. & Garcia, K.C. Structure of the measles virus hemagglutinin. *Nat. Struct. Mol. Biol.* **14**, 1227–1228 (2007).
29. Santiago, C., Bjorling, E., Stehle, T. & Casasnovas, J.M. Distinct kinetics for binding of the CD46 and SLAM receptors to overlapping sites in the measles virus hemagglutinin protein. *J. Biol. Chem.* **277**, 32294–32301 (2002).
30. Toth, J. *et al.* Crystal structure of an ephrin ectodomain. *Dev. Cell* **1**, 83–92 (2001).
31. Stuart, D.I., Levine, M., Muirhead, H. & Stammers, D.K. Crystal structure of cat muscle pyruvate kinase at a resolution of 2.6. *J. Mol. Biol.* **134**, 109–142 (1979).
32. Lawrence, M.C. & Colman, P.M. Shape complementarity at protein/protein interfaces. *J. Mol. Biol.* **234**, 946–950 (1993).
33. Bossart, K.N. *et al.* Functional studies of host-specific ephrin-B ligands as Henipavirus receptors. *Virology* **372**, 357–371 (2008).
34. Pabbisetty, K.B. *et al.* Kinetic analysis of the binding of monomeric and dimeric ephrins to Eph receptors: correlation to function in a growth cone collapse assay. *Protein Sci.* **16**, 355–361 (2007).
35. Li, W. *et al.* Identification of GS 4104 as an orally bioavailable prodrug of the influenza virus neuraminidase inhibitor GS 4071. *Antimicrob. Agents Chemother.* **42**, 647–653 (1998).
36. Altamirano, M.M. *et al.* Ligand-independent assembly of recombinant human CD1 by using oxidative refolding chromatography. *Proc. Natl. Acad. Sci. USA* **98**, 3288–3293 (2001).
37. Walter, T.S. *et al.* A procedure for setting up high-throughput nanolitre crystallization experiments. Crystallization workflow for initial screening, automated storage, imaging and optimization. *Acta Crystallogr. D Biol. Crystallogr.* **61**, 651–657 (2005).

38. Otwinowski, Z. & Minor, W. Processing of X-ray diffraction data collected in oscillation mode. *Methods Enzymol.* **276**, 307–326 (1997).
39. Kabsch, W. Automatic processing of rotation diffraction data from crystals of initially unknown symmetry and cell constants. *J. Appl. Crystallogr.* **26**, 795–800 (1993).
40. McCoy, A.J., Grosse-Kunstleve, R.W., Storoni, L.C. & Read, R.J. Likelihood-enhanced fast translation functions. *Acta Crystallogr. D Biol. Crystallogr.* **61**, 458–464 (2005).
41. Perrakis, A., Harkiolaki, M., Wilson, K.S. & Lamzin, V.S. ARP/wARP and molecular replacement. *Acta Crystallogr. D Biol. Crystallogr.* **57**, 1445–1450 (2001).
42. Collaborative Computational Project, Number 4. The CCP4 suite: programs for protein crystallography. *Acta Crystallogr. D Biol. Crystallogr.* **50**, 760–763 (1994).
43. Brunger, A.T. *et al.* Crystallography & NMR system: a new software suite for macromolecular structure determination. *Acta Crystallogr. D Biol. Crystallogr.* **54**, 905–921 (1998).
44. Murshudov, G.N., Vagin, A.A. & Dodson, E.J. Refinement of macromolecular structures by the maximum-likelihood method. *Acta Crystallogr. D Biol. Crystallogr.* **53**, 240–255 (1997).
45. Adams, P.D. *et al.* PHENIX: building new software for automated crystallographic structure determination. *Acta Crystallogr. D Biol. Crystallogr.* **58**, 1948–1954 (2002).
46. Emsley, P. & Cowtan, K. Coot: model-building tools for molecular graphics. *Acta Crystallogr. D Biol. Crystallogr.* **60**, 2126–2132 (2004).
47. Hooft, R.W., Vriend, G., Sander, C. & Abola, E.E. Errors in protein structures. *Nature* **381**, 272 (1996).
48. Laskowski, R.A., MacArthur, M.W., Moss, D.S. & Thornton, J.M. PROCHECK: a program to check the stereochemical quality of protein structures. *J. Appl. Crystallogr.* **26**, 283–291 (1993).
49. Aricescu, A.R. *et al.* Molecular analysis of receptor protein tyrosine phosphatase μ-mediated cell adhesion. *EMBO J.* **25**, 701–712 (2006).
50. Wallace, A.C., Laskowski, R.A. & Thornton, J.M. LIGPLOT: a program to generate schematic diagrams of protein-ligand interactions. *Protein Eng.* **8**, 127–134 (1995).
51. Corpet, F. Multiple sequence alignment with hierarchical clustering. *Nucleic Acids Res.* **16**, 10881–10890 (1988).
52. Gouet, P., Courcelle, E., Stuart, D.I. & Metoz, F. ESPript: analysis of multiple sequence alignments in PostScript. *Bioinformatics* **15**, 305–308 (1999).